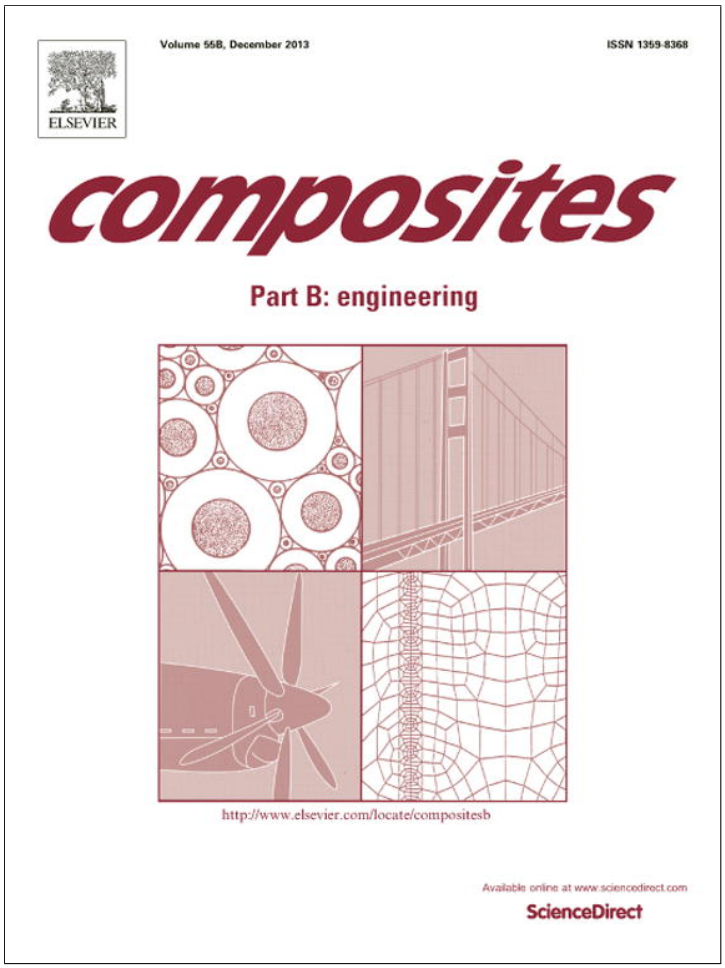

Composites: Part B 55 (2013) 599–606

Contents lists available at ScienceDirect

Composites: Part B

journal homepage: www.elsevier.com/locate/compositesb

The influence of the web-flange junction stiffness on the mechanical behaviour of thin-walled pultruded beams

Francesco Ascione *, Geminiano Mancusi

Dept. of Civil Engineering, University of Salerno, Italy

ARTICLE INFO

Article history:
Received 4 February 2013
Received in revised form 15 May 2013
Accepted 15 July 2013
Available online 24 July 2013

Keywords:
A. Glass fibres
B. Buckling
C. Analytical modelling
E. Pultrusion

ABSTRACT

Composite thin walled members, produced by the manufacturing process of pultrusion, exhibit structural behaviour that is governed by their specific stiffness and strength properties.

Although the basic knowledge about their constitutive behaviour has already been assessed in current technical literature, several relevant features are still being studied. They include the evaluation of the long term behaviour, the influence of the shear deformations, the buckling load as well as the influence of the web-flange junction stiffness.

Due to the presence of unidirectional fibres along the length of the beam, the condition of a rigid connection between the flanges and web panel should be replaced by accounting for possible relative torsional rotations, which can influence the pre-buckling behaviour.

In this paper, a one dimensional mechanical model with the purpose of detecting such an influence is presented. The model, which is based on many common assumptions (a linear kinematics conjugated with small strains and moderate rotations), is innovative in relation to the presence of a few additional degrees of freedom which allow to simulate the web/flange relative rotations, thus generalizing the classical assumptions concerning the generic cross-section which maintains it un-deformed.

Many numerical examples obtained by using a finite element approximation with the aim of highlighting the model capabilities have been developed.

1. Introduction

Over the last few years, FRPs have been used in the field of Civil Engineering for different structural applications, including the restoration of existing concrete [1] and masonry [2,3] members, as well as the erection of new structures entirely made of FRP, such as bridges, footbridges, roof structures and wide membranes.

Within the context of new structures, FRPs are mainly used as pultruded members.

From a mechanical point of view, FRP pultruded profiles can be considered as linear elastic, homogeneous and transversely isotropic, with the plane of isotropy being normal to the longitudinal axis (i.e. the axis of pultrusion). Generally, due to the small thickness, the mechanical behaviour is highly affected by warping strains. In addition, the low values of the shear elastic moduli, more or less the same as the polymeric resin, can provoke a non-negligible increase in terms of lateral deflections, thus affecting both the local and global buckling loads.

Consequently, the design of FRP members is usually driven by deformability and stability requirements which are generally more relevant than the strength limits of the material.

There are numerous studies on both the theoretical and experimental buckling behaviour of members under either axial compressive loads [4–11] or transverse loads [12–19]. A comprehensive study, however, on the influence of the web-flange junction stiffness is still lacking.

The condition under which the pultrusion guarantees a very high strength and stiffness along the longitudinal direction of the beam, while lower structural performances are available with respect to the other directions, suggests the need for a more detailed study on this subject. Moreover, the stiffness of the web/flange connection is expected to be affected by both a higher resin volume fraction as well as a higher risk of local imperfections.

According to the experimental results presented in [20], the stiffness of the web/flange junction can be modelled by a bilinear law which relates the torsional interaction per unit length to the conjugated torsional rotation between the flange and the web. More details are given in the Section 3.3.

From an engineering point of view, two values are thereby relevant: the elastic limit and the ultimate one of the web/flange rotation, with the latter corresponding to the failure of the junction.

* Corresponding author. Tel.: +39 089 968166.
E-mail addresses: fascione@unisa.it (F. Ascione), g.mancusi@unisa.it (G. Mancusi).

1359-8368/$ - see front matter © 2013 Elsevier Ltd. All rights reserved.
http://dx.doi.org/10.1016/j.compositesb.2013.07.021

Within this context, the present paper aims to develop a beam model capable of accounting for the web/flange rotations by assuming the following hypotheses:

(a) the cross-section of the beam is subdivided into a defined number of interconnected thin sub-components;
(b) five degrees of freedom are introduced to simulate the following generalized displacements: the axial displacement (i.e. the displacement of the beam axis along the z direction); the lateral deflections (i.e. the displacements of the beam axis along the x/y directions); the flexural rotations (i.e. the rotations of the cross-section around the x/y axis);
(c) additional degrees of freedom are introduced to simulate the torsional rotation of any sub-component independently from each other;
(d) the strains are assumed to be small, while the flexural/torsional rotations are moderate.

Finally, the basic idea relates to the presence of a separate torsional degree of freedom for any thin sub-component. This feature allows for the web-flange torsional rotation to emerge. In addition, it is also possible to investigate the behaviour of the beam accounting for more general constraints: torsional constraints applied only to the bottom or upper flange as well as to the web panel can be easily simulated by fixing a prescribed value of the corresponding torsional degree of freedom.

The paper is completed by many numerical examples, developed by means of a finite element approximation, which highlight the capabilities of such an approach.

2. Notations

The main relevant symbols utilized are listed below.

$\{\Omega, \mathbf{i}, \mathbf{j}, \mathbf{k}\}$	global reference system
L	beam axis length
B	flange width
H	web depth
b_f	flanges thickness
b_w	web thickness
Σ	generic cross-section
$\Sigma^{(i)}$	intersection between Σ and the ith sub-component
$\Sigma_{(1)}$, $\Sigma_{(2)}$	ends of the beam
O	intersection between the k axis and Σ
P	generic point of the beam
x, y, z	Cartesian components of **P**
x	position vector of the generic point **P**: ($\mathbf{x} = x\mathbf{i} + y\mathbf{j} + z\mathbf{k}$)
u	displacement field
H	displacement gradient
$\boldsymbol{\varepsilon}$	symmetric part of **H**
E	Green strain tensor
S	Cauchy stress tensor
δL_{int}	internal virtual work
δL_{ext}	external virtual work
δL_{con}	virtual work due to the deformability of the web/flange junction
b	external force per unit volume
p	external force per unit surface acting on the boundary of the beam
E	longitudinal Young modulus
G	transverse shear modulus
λ	load multiplier
$(\cdot)^T$	the transposition symbol
$\delta(\cdot)$	the variational symbol
$(\cdot)'$	the derivation symbol with respect to the axial coordinate z

3. Mechanical model

In this section the mechanical model briefly introduced in Section 2 is developed in detail. It is important to note that the model presents a 1-D formulation. In the authors's opinion, this feature fits the main motivations of this study: to propose a user-friendly tool for predicting the behaviour of pultruded members with deformable web/flange junctions overcoming the need for sophisticated approaches relating to 2-D formulations.

3.1. Kinematics

With reference to the generic H-profile shown in Fig. 1, the displacement field assumes the following form:

$$u^{(i)} = u_o - \varphi_3^{(2)} y_o^{(i)} - \varphi_3^{(i)}\left(y - y_o^{(i)}\right) \tag{1.a}$$

$$v^{(i)} = v_o + \varphi_3^{(i)} x \tag{1.b}$$

$$w^{(i)} = w_o + \varphi_1 y - \varphi_2 x \tag{1.c}$$

In Eqs. (1) the index i (i = 1, 2, 3) refers to the generic panel (upper/bottom flange or web), the symbol $\varphi_3^{(i)}$ denotes its own twisting rotation and the symbol $y_o^{(i)}$ indicates the y-coordinate of the centroid of the same panel, assumed as the pole for the rotation $\varphi_3^{(i)}$. Referring to Fig. 1, it results that $y_o^{(1)} = \frac{H}{2}, y_o^{(2)} = 0$ and $y_o^{(3)} = -\frac{H}{2}$.

Five basic generalized displacements are present: u_o, v_o, w_o, φ_1 and φ_2. The symbols u_o, v_o and w_o denote the displacement components of the point **O**, which lies on the beam axis (Fig. 1) and coincides with the centroid of the web panel, while φ_1 and φ_2 denote the flexural rotations of the cross-section around the x and y axis, respectively.

From Eqs. (1.a–c), it easy to express the components of the displacement gradient **H** with reference to the global axes (Fig. 1):

$$H_{11} = 0 \tag{2.a}$$

$$H_{12} = -\varphi_3^{(i)} \tag{2.b}$$

$$H_{13} = u_o' - \varphi_3'^{(2)} y_o^{(i)} - \varphi_3'^{(i)}(y - y_o^{(i)}) \tag{2.c}$$

$$H_{21} = \varphi_3^{(i)} \tag{2.d}$$

$$H_{22} = 0 \tag{2.e}$$

$$H_{23} = v_o' + \varphi_3'^{(i)} x \tag{2.f}$$

$$H_{31} = -\varphi_2 \tag{2.g}$$

$$H_{32} = \varphi_1 \tag{2.h}$$

$$H_{33} = w_o' - \varphi_2' x + \varphi_1' y \tag{2.i}$$

The Green strain tensor thereby assumes the following form:

$$\mathbf{E} = \begin{bmatrix} E_{11} & E_{12} & E_{13} \\ E_{12} & E_{22} & E_{23} \\ E_{13} & E_{23} & E_{33} \end{bmatrix} = \frac{1}{2}\left(\mathbf{H} + \mathbf{H}^{\mathrm{T}} + \mathbf{H}^{\mathrm{T}}\mathbf{H}\right) = \boldsymbol{\varepsilon} + \frac{1}{2}\mathbf{H}^{\mathrm{T}}\mathbf{H} \tag{3}$$

where $\boldsymbol{\varepsilon} = 1/2(\mathbf{H} + \mathbf{H}^T)$.

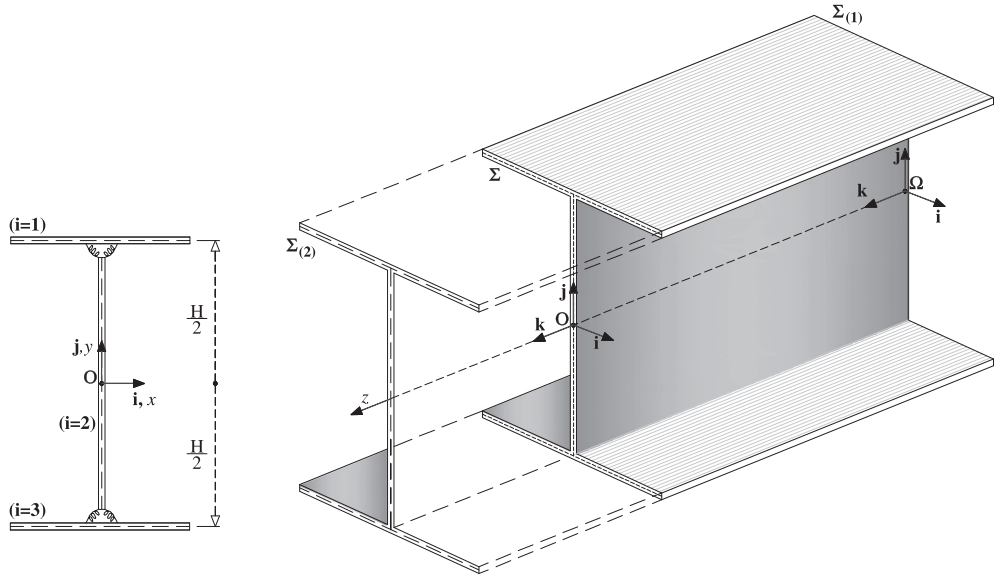

Fig. 1. Beam configuration.

It is worth considering the following comments.

Despite E_{13}, E_{23} and E_{33} being expected to be the only non-trivial strain components, it emerges that so are $E_{11} \neq 0$, $E_{12} \neq 0$, and $E_{22} \neq 0$. This is due to the simplified form of the displacement field. Even if it easy to satisfy the condition $E_{11} = E_{12} = E_{22} = 0$ via more general kinematic assumptions [15], the simplified kinematics proposed in Eqs. (1) has been evaluated as appropriate for practical purposes. Without losing accuracy, the terms E_{11}, E_{12} and E_{22} can be neglected, thus reducing the only non-zero strains to the following:

$$E_{13} = \frac{1}{2}\left[u_o' - \varphi_3^{\prime(2)} y_o^{(i)} - \varphi_3^{\prime(i)}(y - y_o^{(i)}) - \varphi_2 + v_o' \varphi_3^{(i)} + \varphi_3^{\prime(i)} \varphi_3^{(i)} x - \varphi_2 w_o' - \varphi_2 \varphi_1' y + \varphi_2 \varphi_2' x\right] \tag{4.a}$$

$$E_{23} = \frac{1}{2}\left[v_o' + \varphi_3^{\prime(i)} x + \varphi_1 - u_o' \varphi_3^{(i)} + \varphi_3^{\prime(2)} \varphi_3^{(i)} y_o^{(i)} + \varphi_3^{\prime(i)} \varphi_3^{(i)}(y - y_o^{(i)}) + \varphi_1 w_o' + \varphi_1' \varphi_1 y - \varphi_2' \varphi_1 x\right] \tag{4.b}$$

$$\begin{aligned} E_{33} = {} & w_o' - \varphi_2' x + \varphi_1' y \\ & + \frac{1}{2}\left[(u_o')^2 + (v_o')^2 + (w_o')^2 + (\varphi_1')^2 y^2 + (\varphi_2')^2 x^2\right] \\ & + \varphi_3^{\prime(2)} \varphi_3^{\prime(i)} y_o^{(i)}(y - y_o^{(i)}) - u_o' \varphi_3^{\prime(2)} y_o^{(i)} - u_o' \varphi_3^{\prime(i)}(y - y_o^{(i)}) \\ & + v_o' \varphi_3^{\prime(i)} x + w_o' \varphi_1' y - w_o' \varphi_2' x - \varphi_1' \varphi_2' x y \\ & + \frac{1}{2}\left(\varphi_3^{\prime(i)}\right)^2 \left[x^2 + (y - y_o^{(i)})^2\right] + \frac{1}{2}\left(\varphi_3^{\prime(2)}\right)^2 \left(y_o^{(i)}\right)^2 \end{aligned} \tag{4.c}$$

The final expression of the Green Strain tensor as well as its first variation are thereby:

$$\mathbf{E} \cong \begin{bmatrix} 0 & 0 & E_{13} \\ 0 & 0 & E_{23} \\ E_{13} & E_{23} & E_{33} \end{bmatrix} \tag{5}$$

$$\delta\mathbf{E} = \frac{1}{2}\left(\delta\mathbf{H} + \delta\mathbf{H}^{\mathrm{T}} + \delta\mathbf{H}^{\mathrm{T}}\mathbf{H} + \mathbf{H}^{\mathrm{T}}\delta\mathbf{H}\right) \cong \begin{bmatrix} 0 & 0 & \delta E_{13} \\ 0 & 0 & \delta E_{23} \\ \delta E_{13} & \delta E_{23} & \delta E_{33} \end{bmatrix} \tag{6}$$

3.2. Stress–strain relationship

The classical Cauchy tensor **S** has been adopted as a suitable stress measure:

$$\mathbf{S} = \begin{bmatrix} S_{11} & S_{12} & S_{13} \\ S_{11} & S_{22} & S_{23} \\ S_{13} & S_{23} & S_{33} \end{bmatrix} \tag{7a}$$

It is assumed that the stress components are conjugated with the Green strain components through the classical linear elasticity relationships;

$$[S_{13}, S_{23}, S_{33}]^T = \begin{bmatrix} 2G & 0 & 0 \\ 0 & 2G & 0 \\ 0 & 0 & E \end{bmatrix} [E_{13}, E_{23}, E_{33}]^T \tag{7b}$$

where the symbols E and G denote, respectively, the Young modulus along the beam axis and the shear modulus within the (x–z) and (y–z) planes (Fig. 1).

3.3. Web/flange connection

The web/flange junctions are expected to be rotationally deformable. This circumstance, which mainly depends on the unidirectional arrangement of the fibers, can be exacerbated by the presence of resin-rich zones, as highlighted in Fig. 2.

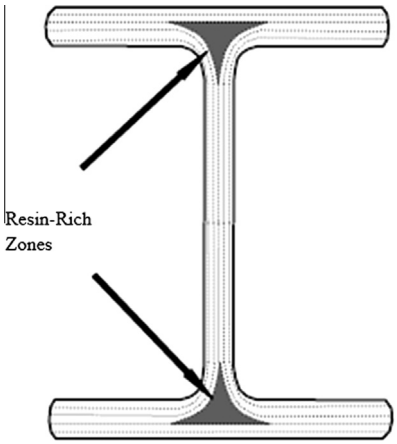

Fig. 2. Resin-rich zones at the web/flange junctions of composite pultruded profiles.

In line with the experimental evidence discussed in [20], the web/flange junctions have been modelled by means of rotational springs (Fig. 1) according to the bilinear law depicted in Fig. 3.

The symbols introduced in Fig. 3 have the following meaning:

$\Delta\varphi_3$	relative web/flange rotation
μ_3	web/flange interaction (per unit length along the beam axis k)
K_1	elastic stiffness parameter
K_2	post-elastic stiffness parameter
$\Delta\varphi_{3,elas}$	maximum elastic rotation
$\Delta\varphi_{3,ult}$	ultimate rotation

The results proposed in [20] have been obtained by Mosallam et al. by means of an innovative experimental set-up shown in Fig. 4.

The experimental tests were performed on both H-profiles and L-profiles made of E-glass fibres embedded in a polyester resin. In order to investigate the desired behaviour, the specimens were held fixed at the lower flange and web, while rotation was applied on the upper flange by means of a rigid steel device.

3.4. Principle of virtual displacement

The virtual work of internal stresses can be expressed as follows:

$$\delta L_{\text{int}} = \sum_{i=1,2,3} \int_0^L dz \int_{\Sigma^{(i)}} [2S_{13}\delta E_{13} + 2S_{23}\delta E_{23} + S_{33}\delta E_{33}] d\Sigma \tag{8}$$

It is worth noting that the internal work δL_{int} accounts for 2nd order terms.

On the other hand, the virtual work done by the external force assumes the following form:

$$\delta L_{ext} = \sum_{i=1,2,3} \int_0^L dz \left[\int_{\Sigma^{(i)}} (\mathbf{b}\delta\mathbf{u}) d\Sigma + \int_{\partial\Sigma^{(i)}} (\mathbf{p}\delta\mathbf{u}) ds \right] + \int_{\Sigma_{(\alpha)}} (\mathbf{p}\delta\mathbf{u}) d\Sigma \tag{9}$$

being:

- $\mathbf{b} = [b_1, b_2, b_3]^T$ the external force field –per unit volume–;
- $\mathbf{p} = [p_1, p_2, p_3]^T$ the external force field acting on the boundary of the beam –per unit surface–;
- $\mathbf{u} = [u, v, w]^T$ the displacement field given by Eqs. (1);
- $\alpha = 1, 2$ an index which refers to the current end of the beam (Fig. 1).

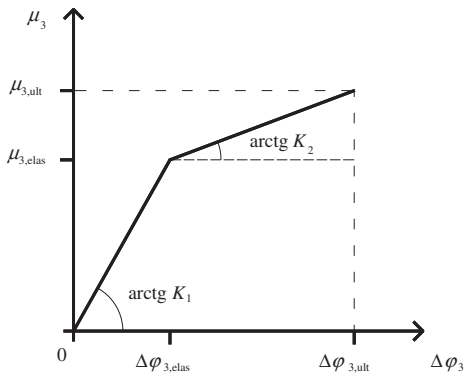

Fig. 3. Relationship between the web/flange relative rotation and the corresponding interaction-per unit length.

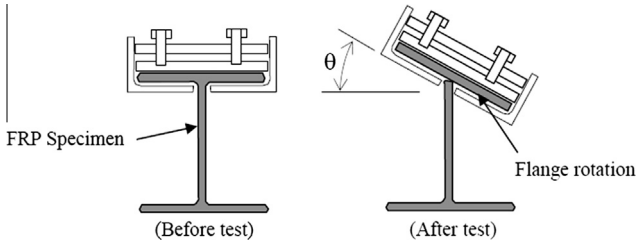

Fig. 4. Experimental set-up followed by Mosallam et al.

Due to the linear form of the displacement field, the 2nd order terms do not emerge in Eq. (9).

It results:

$$\delta L_{ext} = \int_0^L \Big[q_1\delta u_o + q_2\delta v_o + q_3\delta w_o + m_1\delta\varphi_1 + m_2\delta\varphi_2 + \Big(\ldots + m_3^{(i)}\delta\varphi_3^{(i)} + \ldots\Big) + \Big(t_3^{(i)}\delta\varphi_3^{(2)}\Big)\Big] dz + Q_1^{(\alpha)}\delta u_o^{(\alpha)} + Q_1^{(\alpha)}\delta v_o^{(\alpha)} + Q_3^{(\alpha)}\delta w_o^{(\alpha)} + C_1^{(\alpha)}\delta\varphi_1^{(\alpha)} + C_2^{(\alpha)}\delta\varphi_2^{(\alpha)} + \Big(\ldots + C_3^{(\alpha,i)}\delta\varphi_3^{(\alpha,i)} + \ldots\Big) + T_3^{(\alpha,i)}\delta\varphi_3^{(\alpha,2)} \tag{10}$$

with:

$$q_1 = \int_\Sigma b_1 d\Sigma + \int_{\partial\Sigma} p_1 ds \tag{11.a}$$

$$q_2 = \int_\Sigma b_2 d\Sigma + \int_{\partial\Sigma} p_2 ds \tag{11.b}$$

$$q_3 = \int_\Sigma b_3 d\Sigma + \int_{\partial\Sigma} p_3 ds \tag{11.c}$$

$$m_1 = \int_\Sigma b_3 y d\Sigma + \int_{\partial\Sigma} p_3 y ds \tag{11.d}$$

$$m_2 = -\int_\Sigma b_3 x d\Sigma - \int_{\partial\Sigma} p_3 x ds \tag{11.e}$$

$$m_3^{(i)} = \int_{\Sigma^{(i)}} [-b_1(y - y_o^{(i)}) + b_2 x] d\Sigma + \int_{\partial\Sigma^{(i)}} [-p_1(y - y_o^{(i)}) + p_2 x] ds \tag{11.f}$$

$$t_3^{(i)} = -\int_{\Sigma^{(i)}} b_1 y_o^{(i)} d\Sigma - \int_{\partial\Sigma^{(i)}} p_1 y_o^{(i)} ds \tag{11.g}$$

and

$$Q_1^{(\alpha)} = \int_{\Sigma_{(\alpha)}} p_1 d\Sigma \tag{12.a}$$

$$Q_2^{(\alpha)} = \int_{\Sigma_{(\alpha)}} p_2 d\Sigma \tag{12.b}$$

$$Q_3^{(\alpha)} = \int_{\Sigma_{(\alpha)}} p_3 d\Sigma \tag{12.c}$$

$$C_1^{(\alpha)} = \int_{\Sigma_{(\alpha)}} p_3 y d\Sigma \tag{12.d}$$

$$C_2^{(\alpha)} = -\int_{\Sigma_{(\alpha)}} p_3 x d\Sigma \tag{12.e}$$

$$C_3^{(\alpha,i)} = \int_{\Sigma_{(\alpha,i)}} [-p_1(y - y_o^{(i)}) + p_2 x] d\Sigma \tag{12.f}$$

$$T_3^{(\alpha,i)} = -\int_{\Sigma_{(\alpha,i)}} p_1 y_o^{(i)} \mathrm{d}\Sigma \tag{12.g}$$

Finally, the Principle of Virtual Displacements can be expressed as follows:

$$\delta L_{\mathrm{int}} + \delta L_{\mathrm{con}} = \int_0^L \mathbf{q}\delta\mathbf{v}dz + \mathbf{Q}^{(\alpha)}\delta\mathbf{v}^{(\alpha)} \tag{13}$$

where

$$\mathbf{q} = [q_1, q_2, q_3, m_1, m_2, m_3^{(1)}, (m_3^{(2)} + t_3^{(1)} + t_3^{(2)}), m_3^{(3)}]^{\mathrm{T}} \tag{14.a}$$

$$\mathbf{v} = \left[u_o, v_o, w_o, \varphi_1, \varphi_2, \ldots, \varphi_3^{(i)}, \ldots\right]^{\mathrm{T}} \tag{14.b}$$

$$\mathbf{Q}^{(\alpha)} = \left[Q_1^{(\alpha)}, Q_2^{(\alpha)}, Q_3^{(\alpha)}, C_1^{(\alpha)}, C_2^{(\alpha)}, C_3^{(\alpha,1)}, \left(C_3^{(\alpha,2)} + T_3^{(\alpha,1)} + T_3^{(\alpha,3)}\right), C_3^{(\alpha,3)}\right]^{\mathrm{T}} \tag{14.c}$$

$$\mathbf{v}^{(\alpha)} = \left[u_o^{(\alpha)}, v_o^{(\alpha)}, w_o^{(\alpha)}, \varphi_1^{(\alpha)}, \varphi_2^{(\alpha)}, \ldots, \varphi_3^{(\alpha,i)}, \ldots\right]^{\mathrm{T}} \tag{14.d}$$

$$\delta L_{\mathrm{con}} = \sum_{r=1,2} \int_0^L \mu_3^{(r)} \delta\left(\Delta\varphi_3^{(r)}\right) dz \tag{14.e}$$

It is worth noting how the term δL_{con} accounts for the contribution relative to the web/flange interactions $\mu_3^{(r)}$ where the index r refers to the rth web/flange junction ($r = 1, 2$).

3.5. Finite element approximation

Let $\mathbf{u}_{\mathrm{e}}$ be the numeric vector collecting the degrees of freedom related to a generic finite element, with the subscripts "a" and "b" denoting the first and second node, respectively:

$$\mathbf{u}_{\mathrm{e}} = \left[\left(u_o, v_o, w_o, \varphi_1, \varphi_2, \ldots, \varphi_3^{(i)}, \ldots\right)_a, \left(u_o', v_o', w_o', \varphi_1', \varphi_2', \ldots, \varphi_3^{\prime(i)}, \ldots\right)_a, \right.$$
$$\left.(u_o, v_o, w_o, \varphi_1, \varphi_2, \ldots, \varphi_3^{(i)}, \ldots)_b, (u_o', v_o', w_o', \varphi_1', \varphi_2', \ldots, \varphi_3^{\prime(i)}, \ldots)_b\right]^{T} \tag{15}$$

The generalized displacements field $\mathbf{u} = [u_o, v_o, w_o, \varphi_1, \varphi_2, \ldots, \varphi_3^{(i)}, \ldots]^{\mathrm{T}}$ can be interpolated over the generic finite element as follows:

$$\mathbf{u} = \mathbf{N}\mathbf{u}_{\mathrm{e}} \tag{16}$$

In Eq. (16), the symbol $\mathbf{N}$ denotes the following block matrix:

$$\mathbf{N} = [\mathbf{N}_{10}, \quad \mathbf{N}_{11}, \quad \mathbf{N}_{20}, \quad \mathbf{N}_{21}] \tag{17}$$

where

$$\mathbf{N}_{\mathrm{pq}} = \begin{bmatrix} \mathrm{h_{pq}} & 0 & 0 & 0 & 0 & \ldots & 0 & \ldots \\ & \mathrm{h_{pq}} & & 0 & 0 & \ldots & 0 & \ldots \\ & & \mathrm{h_{pq}} & 0 & 0 & \ldots & 0 & \ldots \\ & & & \mathrm{h_{pq}} & 0 & \ldots & 0 & \ldots \\ & & & & \mathrm{h_{pq}} & \ldots & 0 & \ldots \\ & & sym & & & \ddots & 0 & \ldots \\ & & & & & & \mathrm{h_{pq}} & \ldots \\ & & & & & & & \ddots \end{bmatrix} \tag{18}$$

and $\mathrm{h_{pq}}$ are the following cubic Hermitian interpolating functions ($p = 1,2$), ($q = 0,1$):

$$\mathrm{h}_{10} = \frac{1}{4}(2 - 3\xi + \xi^3) \tag{19.a}$$

$$\mathrm{h}_{11} = \frac{l_{\mathrm{e}}}{8}(1 - \xi - \xi^2 + \xi^3) \tag{19.b}$$

$$\mathrm{h}_{20} = \frac{1}{4}(2 + 3\xi - \xi^3) \tag{19.c}$$

$$\mathrm{h}_{21} = \frac{l_{\mathrm{e}}}{8}(-1 - \xi + \xi^2 + \xi^3) \tag{19.d}$$

being ξ the normalized axial coordinate ($-1 \leqslant \xi \leqslant 1$) and l_{e} the length of the current finite element.The internal stresses can be expressed as a function of the nodal displacements by means of:

$$[S_{13}, S_{23}, S_{33}]^{\mathrm{T}} = \mathbf{C}(\mathbf{B}_{\mathrm{L}} + \mathbf{u}_{\mathrm{e}}^T\mathbf{B}_{\mathrm{NL}})\mathbf{u}_{\mathrm{e}} \tag{20}$$

where S_{13}, S_{23} and S_{33} denote the internal stresses given in Eq. (7b), $\mathbf{C}$ accounts for the elastic moduli while $\mathbf{B}_{\mathrm{L}}$ and $\mathbf{B}_{\mathrm{NL}}$ account for the linear and non-linear part of the strain field, respectively. In particular, it results:

$$\mathbf{C} = \begin{bmatrix} (2G/\chi) & 0 & 0 \\ 0 & (2G/\chi) & 0 \\ 0 & 0 & E \end{bmatrix}, \tag{21}$$

where the term (G/χ) denotes the shear modulus with χ the cross-section corrective factor, while the term E indicates the Young modulus along the k-axis.The secant stiffness matrix $\mathbf{K}_{\mathrm{e}}$ assumes the following final form, where the subscript "e" refers to a generic finite element:

$$\mathbf{K}_{\mathrm{e}} = \frac{l_e}{2}\int_{-1}^{+1} \mathbf{B}^{\mathrm{T}}\mathbf{C}\mathbf{B}d\xi + \sum_{r=1,2}\frac{l_e}{2}\int_{-1}^{+1} \mathbf{N}^T\mathbf{d}^{(r)T}K_{\mathrm{sec}}\mathbf{d}^{(r)}\mathbf{N}d\xi. \tag{22}$$

In Eq. (22), the following positions have been introduced:

$$\mathbf{B} = \mathbf{B}_{\mathrm{L}} + \mathbf{u}_{\mathrm{e}}^T\mathbf{B}_{\mathrm{NL}}, \tag{23.a}$$

$$\mathbf{d}^{(r)} = \mathbf{d}^{(i)} - \mathbf{d}^{(j)} \tag{23.b}$$

with $r = 1, 2$ and K_{sec} denoting the secant stiffness of the rth web/flange junction.

In Eq. (23.b), the symbols $\mathbf{d}^{(i)}$ and $\mathbf{d}^{(j)}$ denote two numeric vectors which exhibit null components except for the twisting degree of freedom relative to the ith and jth sub-component, respectively. By virtue of this position, the relative torsional rotation between the ith and jth sub-component can be expressed by the following row by column product: $\mathbf{d}^{(r)}\mathbf{u}$.By standard procedures, the equilibrium equations of the finite element model can be written as follows:

$$\mathbf{K}_{\mathrm{g}}\mathbf{U}_{\mathrm{g}} = \mathbf{F} \tag{24}$$

where $\mathbf{K}_{\mathrm{g}}$ is the global secant stiffness matrix, $\mathbf{U}_{\mathrm{g}}$ and $\mathbf{F}$ denote the nodal global displacements and external forces vectors in the reference system $\{\Omega, \mathbf{i}, \mathbf{j}, \mathbf{k}\}$, respectively.

4. Numerical results

In this section, some numerical results concerning a composite H-profile are presented and discussed.

The goals are the following:

- the assessment of the proposed approach by comparing the numerical predictions with other results presented in literature;
- the evaluation of the influence of the external torsional constraints, which can be applied to either the whole cross-section or the upper/bottom flange only, as well as the web;
- the evaluation of influence of the web/flange junction stiffness;
- the evaluation of the influence of the shear deformability of the flanges and/or the web.

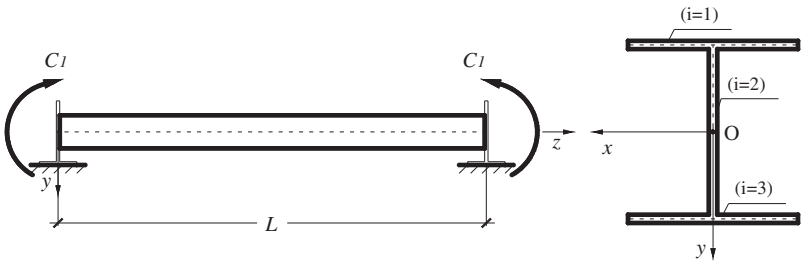

Fig. 5. Structural scheme.

Table 1
Mechanical and geometrical properties.

Shape	E (MPa)	G (MPa)	B (mm)	H (mm)	$b_f = b_w = b$ (mm)	L (mm)
200 × 200 × 10	18633	4428	200	190	10	1900
200 × 200 × 10	18633	4428	200	190	10	6000

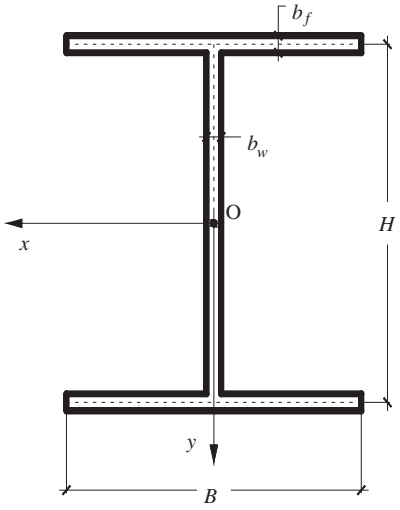

Fig. 6. Dimensions of the cross-section.

4.1. Model assessment

The first scheme examined by the authors concerns the GFRP H-profile shown in Fig. 5. The beam is simply supported with supports preventing the torsional rotations of both the flanges and web.

The geometrical and mechanical properties are summarized in Table 1. The cross-section is depicted in Fig. 6.

A constant bending moment C_1 is attained over the beam axis.

This scheme, already considered in [21–24], has been here reproduced in view of a preliminary comparison.

In order to accommodate the mechanical hypotheses assumed in [21,23], the model presented in Section 3 has been applied in combination with the following choices:

(a) both the flanges and web have been assumed shear deformable only in the plane between the z-axis and the current tangent to the mid-line, while shear un-deformability has been considered in the plane between the z-axis and the normal to the mid-line.
(b) the stiffness of the web/flange junctions has been increased towards infinite.

Table 2
Buckling loads – comparison.

Shape	L (mm)	$C_{1,CR(R)}$ (k Nm)	$C_{1,CR(A)}$ (k Nm)	$C_{1,CR(PM)}$ (k Nm)
200 × 200 × 10	1900	78.60	73.39	76.00
200 × 200 × 10	6000	11.90	10.80	17.00

(PM) present model.

Table 3
Convergence tests.

Mesh refinement	Convergence test 1 – L = 1900 mm		Convergence test 2 – L = 6000 mm	
	Finite elements	$\varphi_3^{(2)} \times 10^{+6}$	Finite elements	φ_1
#1	50	−2.5689	1000	−0.02013
#2	100	−2.5625	1500	−0.01343
#3	200	−2.5554	2000	−0.01008
#4	500	−2.5545	3000	−0.00672
#5	600	−2.5545	3500	−0.00672

The comparison has been reported in terms of the buckling load (i.e. the critical value of the external moments applied to the ends of the beam), with the numerical results being summarized in Table 2.

The prediction obtained by the present model ($C_{1,CR(PM)}$) has been compared with the buckling loads given in [21] ($C_{1,CR(R)}$) and in [23] ($C_{1CR(A)}$).

Despite the strategy followed in [23] (i.e. eigenvalue problem), the value $C_{1,CR(PM)}$ has been obtained as the asymptotic limit of the non-linear response evaluated via the numerical model discussed in Section 3.5. An imperfection has been included in terms of a small initial deflection along the x-axis.

The accuracy of the mesh adopted (Table 3) has been checked *a posteriori* with respect to the torsional rotation of the web panel, $\varphi_3^{(2)}$ for beam with L = 1900 mm, and flexural rotation, φ_1 for the beam with L = 6000 mm. Both the monitored values have been evaluated at the mid-span cross-section under the critical value of the external moment.

Table 4
Mechanical and geometrical properties.

E (MPa)	G (MPa)	B (mm)	H (mm)	b_f (mm)	b_w (mm)
23000	3000	100	196	8	5

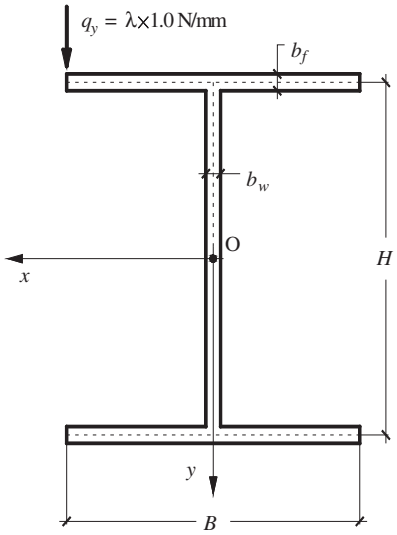

Fig. 7. Cross-section under investigation.

It is worth noting that there is a good agreement with the results presented in current literature in the case of the less slender beam.

4.2. Influence of the kinematic boundary conditions

With the aim of highlighting the influence of the kinematical boundary conditions on the pre-buckling behaviour of a simply supported GFRP beam with H-profile, the authors have considered a new beam cross-section (both for geometrical and mechanical properties) with respect to the previous Section 4.1. The aforementioned properties are summarized in Table 4.

The analysis has been carried out taking into account:

- four different values of L (length of the beam): 1000 mm, 2000 mm, 3000 mm and 4000 mm;
- two different choices concerning the torsional constraints applied at the ends of the beam: the first one, called "FFC", corresponds to the following condition: $\varphi_3^{(1)} free, \varphi_3^{(2)} free, \varphi_3^{(3)} = 0$ (i.e. only the torsional rotation of the bottom flange is prevented), while the other one, "CCC", corresponds to $\varphi_3^{(1)} = \varphi_3^{(2)} = \varphi_3^{(3)} = 0$ (the torsional rotations of both the web panel as well as the upper and bottom flanges are prevented);
- a uniform eccentric load per unit length applied as depicted in Fig. 7;
- two different relationships to model the web/flanges junction by means of rotational springs (Fig. 1): the first one is the bilinear relationship depicted in Fig. 3; the second one is a simplified linear relationship obtained by assuming the secant stiffness at failure. The relationship parameters are summarized in Table 5.

The results are plotted in Fig. 8 in terms of the critical load multipliers λ versus beam length, L, related to the above cited FFC and CCC kinematic boundary conditions.

Table 5
Mechanical parameters of the web/flange connection relationship.

Web/flange junction model	$\Delta\varphi_{3,elas}$ (rad)	$\Delta\varphi_{3,ult}$ (rad)	K_1 (N mm/mm)	K_2 (N mm/mm)
M 1	0.04	0.3	7,500,000	400,384
M 2	0.3	0.3	1,347,000	–

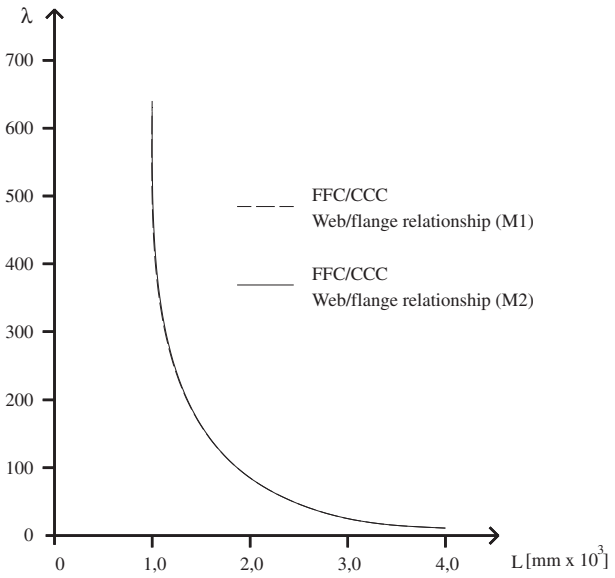

Fig. 8. Influence of constraint conditions and junction relationships on the load multiplier λ.

It is worth considering the following considerations.

First of all, as previously stated, the critical value of λ has been evaluated by detecting the asymptote of the non-linear response of the numerical model.

From the graph of Fig. 8, it is possible to understand that the kinematical boundary conditions do not influence the beam buckling load. The comparison between the numerical results obtained by the relationships M1 and M2 do not show any relevant differences, thus allowing to simplify the experimental characterization of the junction behaviour.

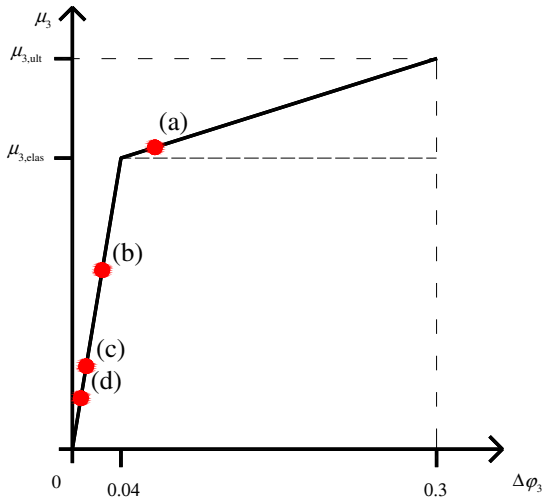

Fig. 9. Web-flange rotations at the buckling point [L = 1000 mm (a) L = 2000 mm (b) L = 3000 mm (c) L = 4000 mm (d)].

Table 6
Critical values of λ.

L (mm)	λ	
	G = 3000 MPa	$G \to \infty$
1000	640	1000
2000	85	100
3000	25	26
4000	12	12

4.3. Influence of the deformability of the web/flange connection

The entity of web/flange relative rotations has been investigated with reference to the same scheme previously considered in Section 4.2.

The constraint condition named "FFC" has been considered due to the circumstance that the main effects emerge at the ends of the beam where $\Delta\varphi_3^{(23)} = \varphi_3^{(2)} - \varphi_3^{(3)}$ with $\varphi_3^{(3)} = 0$. The results have been presented in Fig. 9 with reference to several length values for the corresponding critical values of the load multiplier.

It is possible to understand for the low slenderness beam the elastic limit ($\Delta\varphi_{3,elas}$) appears before the buckling load is reached.

It is worth noting that the possibility to capture this last result is particular to the mechanical model presented here.

4.4. Influence of shear deformability

The influence of the shear deformability on the buckling has been investigated with reference to the same scheme previously considered in Sections 4.2 and 4.3.

In this example, only the constraint condition named "FFC" has been considered. Limiting our discussion to the junction model M1, the numerical results are reported in Table 6 in terms of the critical values of the load multiplier λ .

The results reveal that the simplified model proposed by the authors is able to account for a relevant influence of the shear deformability of the web and flanges on the global buckling limit, especially for a short length beam.

5. Conclusions

This paper deals with the formulation of a simplified mechanical model with the purpose of detecting the influence of the web/flange junction stiffness on the pre-buckling behaviour of pultruded composite beams.

The main feature of the model is to adopt an innovative 1-D formulation which allows to predict the aforementioned influence instead of using more complex 2-D analyses.

The present model has been derived from the classical Timoshenko's beam formulation by including a few additional degrees of freedom capable of simulating the web/flange relative rotations. This is based on the choice of subdividing the cross-section into sub-components (i.e. the flanges, the web panel) which can exhibit a local torsional rotation field.

The stiffness of the web/flange junction has been modelled according to recent results presented in current literature relating the web/flange relative rotation and the conjugated interaction per unit length. This relationship is assumed to be bilinear and depends on a few parameters: the elastic limit and ultimate limit of the relative web/flange rotation, the elastic and post-elastic stiffnesses.

Many numerical results have been obtained by means of a finite element discretization in order to highlight the capabilities of the model, which deal with the influence of the junction stiffness, but also with the possibility of prescribing separate torsional constraints on any sub-component.

The numerical results, relative to the H-profile subjected to eccentric vertical load, have shown that when dealing with low slenderness beams, it emerges that the elastic limit of the web/flange rotation can be attained before the buckling load is reached. This last result represents a particularity of the proposed mechanical model.

Finally, this suggests the need for the manufacturer to perform a mechanical characterization of the web/flange junction stiffness. The authors have also shown that it is possible to obtain the characterization of the web/flange junction relationship by means of a simplified test intended to detect only the ultimate point of the relationship. This could be useful for technical purposes, due to the possibility to overcome the complexity of a full identification of all the parameters of the bilinear relationship.

References

[1] Benzarti K, Freddi F, Frémond M. A damage model to predict the durability of bonded assemblies. Part I: debonding behaviour of FRP strengthened concrete structures. Constr Build Mater 2011;25(2):547–55.
[2] Baratta A, Corbi O. Stress analysis of masonry vaults and static efficacy of FRP repairs. Int J Solids Struct 2007;44(24):8028–56.
[3] Corbi I. FRP composites retrofitting for protection of monumental and ancient constructions. Open Constr Build Technol J 2012;6:361–7.
[4] Turvey GJ, Zhang Y. A computational and experimental analysis of buckling, post buckling and initial failure of pultruded GRP columns. Comput Struct 2006;84:1527–37.
[5] Mottram JT. Determination of critical load for flange buckling in concentrically loaded pultruded beams. Composites: Part B 2004;35(1):35–47.
[6] Di Tommaso A, Russo S. Shape influence in buckling of GFRP pultruded columns. Mech Compos Mater 2003;39(4):329–40.
[7] Qiao P, Davalos J, Wang J. Local buckling of composites FRP shapes by discrete plate analysis. ASCE J Struct Eng 2001;127(3):245–55.
[8] Kollar LP. Local buckling of fiber reinforced plastic composite structural members with open and closed cross sections. ASCE J Struct Eng 2002;129(11):245–55.
[9] Minghini F, Tullini, Laudiero F. Buckling analysis of FRP pultruded frames using locking-free finite elements. Thin Wall Struct 2008;46:223–41.
[10] Pecce M, Cosenza E. Local buckling curves for the design of FRP profiles. Thin Wall Struct 2000;37(33):207–22.
[11] Qiao P, Shan L. Explicit local buckling analysis and design of fiber-reinforced plastic composite structural shapes. Compos Struct 2005;70:468–83.
[12] Mittelstedt C. Local buckling of wide-flange thin-walled anisotropic composite beams. Arch Appl Mech 2007;77:439–52.
[13] Feo L, Mancusi G. Modeling shear deformability of thin-walled composite beams with open cross section. Mech Res Commun 2010;37(3):320–5.
[14] Feo L, Mancusi G. The influence of the shear deformations on the local stress state of pultruded composite profiles. Mech Res Commun 2013;47(1):44–9.
[15] Mancusi G, Feo L. Non-linear pre-buckling behaviour of shear deformable thin-walled composite beams with open cross-section. Composites: Part B 2013;47:379–90.
[16] Ferreira AJM, Carrera E, Cinefra M, Roque CMC, POLIT O. Analysis of laminated shells by a sinusoidal shear deformation theory and radial basis functions collocation, accounting for through-the thickness deformations. Composites: Part B 2011;42:1276–84.
[17] Bourgeois S, Cochelin B, Guinot F, Picault E. Buckling analysis of tape springs using a rod model with flexible cross-sections. Eur J Comput Mech 2012;21:184–94.
[18] Guinot F, Bourgeois S, Cochelin B, Blanchard L. A planar rod model with flexible thin-walled cross-sections. Application to the folding of tape springs. Int J Solids Struct 2012;49:73–86.
[19] Feo L, Mosallam AS, Penna R. Mechanical behaviour of web-flange junctions of thin walled pultruded I-profiles: an experimental and numerical evaluation. Composites: Part B 2013;48:18–39.
[20] Mosallam AS, Elsadek AA, Pul S. SemH-rigid behaviour of web-flange junctions of open-web pultruded composites. In: Proceedings of the international conference on FRP composites. San Francisco, California; 2009.
[21] Roberts TM, Al-Ubaidi H. Influence of shear deformation on restrained torsional warping of pultruded FRP bars of open cross-section. Thin Wall Struct 2001;39:395–414.
[22] Roberts TM. Influence of shear deformation on buckling of pultruded fiber reinforced plastic profiles. J Compos Constr 2002;6(4):241–8.
[23] Ascione L, Giordano A, Spadea S. Lateral buckling of pultruded FRP beams. Composites: Part B 2011;42(4):819–24.
[24] Ascione L, Berardi VP, Giordano A, Spadea S. Buckling failure modes of FRP thin-walled beams. Composites: Part B 2011;42(4):819–24.